

# Determining suspended sand size and concentration from multifrequency acoustic backscatter

A. M. Crawford and Alex E. Hay

Department of Physics, Memorial University of Newfoundland, St. John's, Newfoundland A1B 3X7, Canada

(Received 27 May 1993; accepted for publication 19 July 1993)

An inversion algorithm for extracting suspended sand size and concentration from simultaneous backscattered acoustic pressure amplitude at three operating frequencies is presented. The algorithm is based on the differences in signal amplitude between different frequency pairs, and is tested using laboratory measurements of multifrequency backscatter from a turbulent sediment-carrying jet. Concentration and size profiles inverted from field and laboratory data are compared with results from a previously developed algorithm based on signal ratios. The difference inversion scheme is less sensitive to errors arising from low signal levels, allowing the size/concentration measurement range to be extended to regions of lower concentration. The concentrations from the field data agree well with independent optically determined estimates. The results demonstrate sensitivity to the backscatter form factor.

PACS numbers: 43.30.Gv, 43.30.Ft

## INTRODUCTION

Acoustic imaging has proven effective for monitoring suspended sediment in the nearshore zone.<sup>1-7</sup> This is a particularly demanding environment, requiring nonintrusive apparatus, high temporal and spatial resolution, and equipment of robust construction. Single-frequency acoustic methods have been successful, but have shortcomings that are inherent in the dual dependence of the backscattered signal on the concentration and size of the scatterers.<sup>3,4,7</sup> Multifrequency techniques offer the possibility of measuring particle size simultaneously with concentration at fixed points, or as a function of range. Determination of particle size is relevant to the dynamics of sediment suspension, but measurement of size has not been common in the context of nearshore sediment studies.<sup>8,9</sup>

Previous work<sup>10,11</sup> with the multifrequency RAS-TRAN (Remote Acoustic Sediment TRANsport measurement) system led to an inversion method for extraction of sand size and concentration from the multifrequency backscatter data. This so-called ratio algorithm<sup>10,11</sup> matches ratios of measured signal levels to precalculated theoretical values which are a function of size. A primary failing of this algorithm<sup>10</sup> is that at low scatterer concentrations, low signal levels (particularly in the denominator of a ratio) contribute to increased noise level in the inverted results. An alternative method is presented here which, by using the differences between signal levels, is less prone to noise in regions of low scatterer concentration.

This paper contains a description of the new inversion method and results from laboratory and field experiments. The inverted sizes and concentrations from the laboratory experiments are compared to physical measurements of these quantities and concentrations determined from the field data are compared to optical measurements. Comparison to results obtained using the ratio algorithm are also presented.

Proper extraction of the size information from the multifrequency data by any method requires prior knowledge of the size/frequency dependence of the backscatter signal. Factors such as the material composition of the scatterers can introduce variation in the scattering cross section, even locally. The sensitivity of inverted results to small differences in the backscatter form factor is investigated. In addition, it is necessary to know the effect of attenuation of the signal by scatterers. Measurements and discussion of scattering attenuation are presented in the Appendix.

## I. MEASUREMENT TECHNIQUE

The multifrequency acoustic backscatter system, RAS-TRAN system 1, has been described in detail elsewhere.<sup>10,12</sup> The transceivers operate at three frequencies (1, 2.25, and 5 MHz), and over a range of about 1 m. Data from each of the units is logged on a CAMAC-crate and PC-based data acquisition system.<sup>12,13</sup>

In the laboratory studies,<sup>13</sup> an axisymmetric region of statistically steady scatterer concentration is maintained by a recirculating jet carrying sand of known size. Independent concentration measurements are obtained by syphon between acoustic runs. The beams intersect at the center of the jet 28 cm downstream from the nozzle, 55 cm away from the three transceivers. Backscatter profiles across the jet were acquired at a rate of 6.6 Hz, with four-ping ensemble averaging and block averaging of three adjacent sample points. In this mode, the range resolution was 1.1 cm. Experiments were performed using natural beach sand from three locations, described in Table I, and with sieved samples. Size fractions were separated into quarter-phi intervals between 98  $\mu\text{m}$  ( $d_{50}$ ) and 463  $\mu\text{m}$  using standard sieving techniques<sup>14</sup> (particle size in mm is given by  $2^{-\text{phi}}$  on the phi scale). The size distribution of the unsieved samples was log-normal.

TABLE I. Size distribution parameters for natural sand used in laboratory experiments.  $d_{50}$  is the median diameter by weight and  $d_{16}$  and  $d_{84}$  are the diameters of the 16th and 84th percentile in the cumulative size distribution:  $\sigma_g$  is the width of the log-normal size distribution.

Location	$d_{50}$ ( $\mu\text{m}$ )	$d_{16}$ ( $\mu\text{m}$ )	$d_{84}$ ( $\mu\text{m}$ )	$\sigma_g$
Bluewater Beach (BWB)	139	111	171	1.30
Stanhope Lane Beach (PEI)	157	129	189	1.25
Queensland Beach (QLB)	360	275	460	1.35

Figure 1 shows the field deployment of RASTRAN at Stanhope Lane Beach, Prince Edward Island in October–November of 1989. Four transceivers operating at the three frequencies were mounted looking downward, as shown. The 20-cm separation of the units is larger than the beam-width and was chosen for observation of concentration fluctuation transit times.<sup>15</sup> The system collected profiles at a rate of 6.6 Hz. Each profile was a four-ping ensemble average and had five adjacent sample points averaged giving a vertical resolution of 1.8 cm. Simultaneous concentration measurements were made using Optical Backscatter Sensors (OBS) and logged at 4.55 Hz on the separate UDATS system<sup>16</sup> for 1/2-h periods usually overlapping four 6.5-min RASTRAN runs. Field data to be presented here were logged on 4 different days, as listed in Table II. Conditions on these days separate the runs into high (H), intermediate (I) and low (L) energy<sup>10</sup> by relative surface gravity wave energy.

A RASTRAN data file consists of a series of *sets* (typically 200 for a laboratory run and 2600 for a field run). Each set contains the four-ping, ensemble-averaged, profiles for each of the frequency channels. Each four-ping ensemble profile is subdivided into *bins* representing range dependence. In preprocessing, small differences in the distance-to-bottom, or distance-to-jet-center, between the transducer units are corrected numerically by shifting the entries in the respective channels by the appropriate number of range bins. Averaging is an important aspect of the signal preprocessing, and will be discussed later. Background level, removed from the raw voltage data, is determined by averaging 50 “quiet” profiles from time periods when suspended sediment concentrations are negligible or, in the laboratory, from a run with no sand in the recirculating system.

## II. THEORY

The following section contains a brief discussion of the theory of acoustic backscatter detection systems. More detailed versions of this treatment can be found elsewhere.<sup>10,13</sup>

Consider a pulsed monostatic system detecting acoustic pressure which has been backscattered from objects in the path of the transmitted beam. Assume that the scatterers are randomly and homogeneously distributed across the detected volume defined by the main lobe of the transducer beam and  $r_0 \pm c\tau/4$ , where  $c$  is the sound speed and

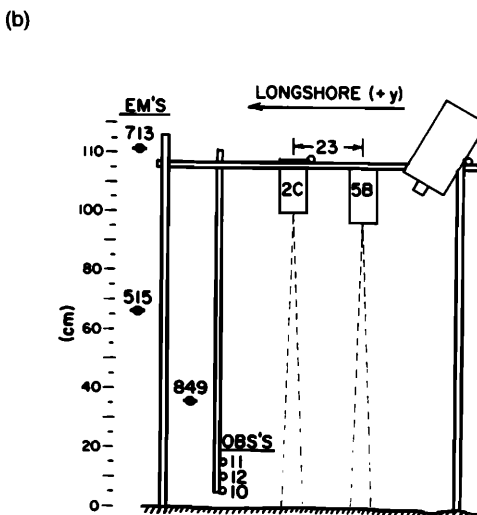
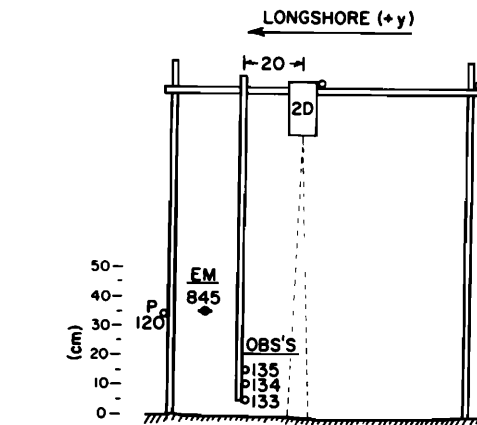
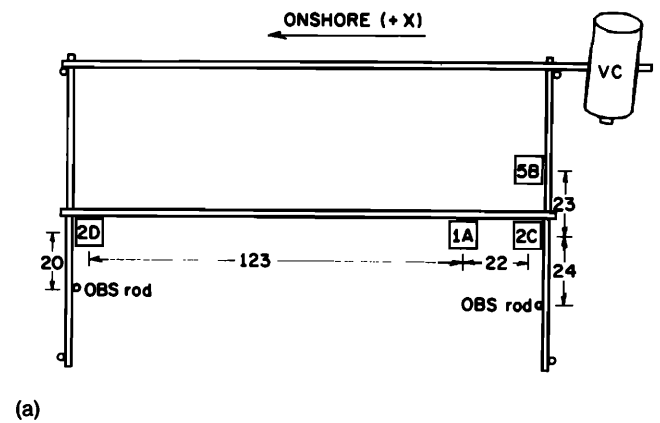


FIG. 1. Plan (a), and end views (b) and (c) of the RASTRAN measurement system I as deployed in the field experiment at Stanhope Lane, Prince Edward Island, in October–November of 1989. VC is a video camera and EM are electromagnetic current meters. P is a pressure sensor. The transceivers labeled 1A, 2C, and 5B operate at 1, 2.25, and 5 MHz, respectively.

$\tau$  is the pulse length. Acoustic waves returning to the transducer are assumed to be incoherent from pulse to pulse.

Assuming dilute scatterers with density  $\rho_0'$ , then the mean-squared voltage returned is given by

TABLE II. RASTRAN data files selected for comparisons. Run number is the Julian day followed by the consecutive number of the run during that day.  $U_{1/3}$  is the significant wave orbital velocity, and  $T_p$  is the wave period at the main peak of the energy spectrum.

Run number	$U_{1/3}$ (m/s)	$T_p$ (s)
299.025-.028 (I)	0.57	4.3
300.030 (L)	0.33	5.1
300.040 (L)	0.28	5.1
301.015 (I)	0.43	3.7
308.046,.047 (H)	0.77	6.2

$$\langle v^2 \rangle = S_M^2 \frac{|f_\infty|^2 c \tau M_0}{a_0} \frac{e^{-A} \sinh B}{2 \rho'_0 B}, \quad (1)$$

where  $S_M$  is an empirically determined system sensitivity constant,  $|f_\infty|$  is the far-field backscattering form factor for a freely moving scatterer, and  $a_0$  and  $M_0$  are the mean scatterer radius (midpoint of the sieve interval) and concentration within the detected volume. Also,

$$A = 4\Delta_0 = 4 \int_0^{r_0} \alpha_s dr \quad (2)$$

and

$$B = (\alpha_w + \alpha_{s0}) c \tau, \quad (3)$$

where  $\alpha_w$  is the linear attenuation coefficient for water and  $\alpha_s$  is a scattering attenuation coefficient. The subscript 0 refers to values associated with a particular detected volume centered at range  $r_0$ . The term  $e^{-4\alpha_w r_0 / r_0^2}$  has been dropped from the expression since the voltage output from the transducers is corrected for spherical spreading and attenuation due to water. [This is done in the transceivers by time variable gain (TVG) amplification using factory-set values for  $\alpha_w$  and  $c$ . A recorection is applied to the data prior to processing using *in situ* temperature and salinity values.] The terms  $e^{-A} \sinh B/B$  correct for attenuation of the acoustic transmission by the scatterers themselves, and will be discussed further later.

The assumptions made in the derivation of Eq. (1) are not limiting in most cases. Laboratory measurements show a linear dependence of attenuation on scatterer concentration up to 30 g/liter (1% by volume), indicating that the single scattering assumption is valid up to that concentration.<sup>13</sup> The effect of nonuniform mean scatterer concentration within the detected volume for the jet experiments has been discussed elsewhere,<sup>13</sup> and has not been considered in the present calculations.

Estimates of concentration and size can be obtained from Eq. (1) only after the calibration factor  $S_M$  has been determined and the frequency/size dependence of the backscattering form factor  $|f_\infty|$  is known. The calibration procedure used for this system involved backscatter measurements made with glass beads<sup>13</sup> of known acoustic characteristics.<sup>17</sup>

### A. The backscattering form factor— $|f_\infty(X)|$

Sheng<sup>11</sup> proposed that the theoretical backscattering form factor for spherical quartz particles could be modified

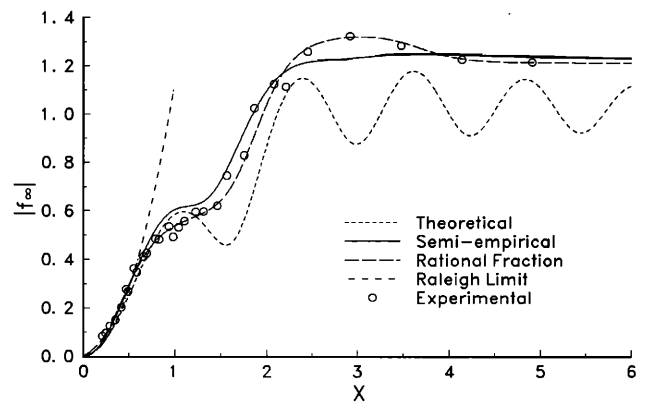


FIG. 2. Backscattering form factor,  $|f_\infty|$ , for natural sand grains in water. Shown are the theoretical form factor for spherical quartz grains (short-dashed line), the semiempirical form factor (solid line), the rational fraction fit to data (long-dashed line), the Raleigh (small  $\times$ ) limit dependence, and measured values ( $\circ$ ).

to fit experimental form factor data for natural sand grains. Figure 2 shows measured values for  $|f_\infty|$  for sand, taken from experiments performed with the suspended sediment jet.<sup>13</sup> The medium-dashed line in Fig. 2 is Sheng's<sup>11</sup> semiempirical form factor, given by

$$|f_{\infty s}|^2 = \frac{(1 + 1.25X^4)^2}{(1 + X^4)^2} \left( \frac{a \int_0^\infty a^2 |f_\infty|^2 n(a) da}{\int_0^\infty a^3 n(a) da} \right), \quad (4)$$

where  $n(a)$  is the distribution function for size,  $|f_\infty|$  is the theoretical form factor for rigid, movable scatterers<sup>18</sup> (the short-dashed line), and  $X = ka$ . A log-normal distribution was assumed for  $n(a)$ , with  $\sigma_g = 1.2$ ; i.e.,

$$n(a) = \frac{1}{\sqrt{2\pi \ln \sigma_g}} \exp\left(-\frac{(\ln a - \ln a_g)^2}{2 \ln^2 \sigma_g}\right) \quad (5)$$

where  $a_g$  is the geometric mean radius and  $\ln^2 \sigma_g$  is the variance of  $\ln a$ . In Eq. (4), the term in square brackets is a smoothing factor, while the leading term is a vertical stretching coefficient. The oscillations evident in the purely theoretical form factor for spherical particles are not seen in the experimental data, which were determined from narrow-band backscatter experiments using natural sand particles.<sup>13</sup> The experimental form factor data are supported by broadband acoustic backscatter measurements performed under similar conditions.<sup>19</sup>

An alternative approach is to obtain a purely empirical result. An accurate fit is obtained using a rational fraction fit<sup>20</sup> to the data:

$$|f_{\infty r}(X)| = \frac{0.6 + 1.33[X/1.91]^{10}}{1 + [X/1.91]^{10}} \frac{0.4X + [X/0.6]^3}{1 + [X/0.6]^3} \times \frac{1 + 0.91[X/3.7]^{16}}{1 + [X/3.7]^{16}}, \quad (6)$$

shown in Fig. 2 (long-dashed line). As can be seen from the figure, the fit accurately represents the data over the full range of the measurements,  $X < 4$ . [Note that this fit does not exhibit the Rayleigh ( $X^2$ ) dependence for  $X \ll 1$ . As shown in the figure, however, the rational fraction and

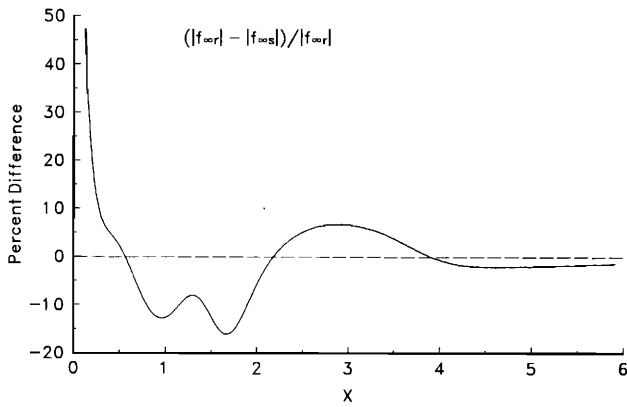


FIG. 3. Percent difference between the rational fraction fit form factor and the semiempirical form factor.

parabolic curves are nearly identical for  $0.2 < X < 0.5$ .] The percentage difference between the rational fraction and semiempirical fits is shown in Fig. 3.

### B. Scattering attenuation correction

Particles suspended in the ambient fluid contribute to the attenuation of acoustic energy. Areas of high scatterer concentration distort the view of particles behind. The magnitude of this effect depends on the size and concentration of the scatterers and the backscatter data must be corrected for this before inversion.

Sheng and Hay<sup>21</sup> suggested that a modified form of the "high-pass model" for backscattering intensity proposed by Johnson<sup>22</sup> leads to a suitable approximation for the scattering attenuation. Using this idea,

$$\frac{a\alpha_s}{\epsilon} = \frac{\kappa_\alpha X^4}{[1 + \frac{4}{3}\kappa_\alpha X^4 + X^2]}, \quad (7)$$

where

$$\kappa_\alpha = \frac{\gamma_\kappa^2 + \gamma_\rho^2/3}{6}, \quad \gamma_\kappa = \frac{\kappa'_* - \kappa}{\kappa}, \quad \text{and} \quad \gamma_\rho = \frac{3(\rho'_0 - \rho_0)}{2\rho'_0 + \rho_0}.$$

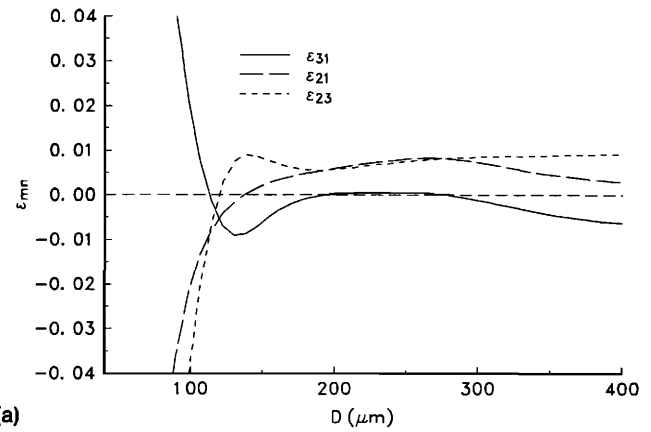
Primed quantities refer to the scatterers and unprimed to the fluid medium.  $\kappa'_*$  is the scatterer bulk compressibility, given by  $[\lambda' + 2\mu'/3]^{-1}$ , where  $\lambda'$  and  $\mu'$  are the Lamé constants;  $\kappa$  and  $\rho$  are the bulk compressibility and density of water; and  $\epsilon = M/\rho'_0$  is the volume concentration of scatterers. For quartz in water,  $\kappa_\alpha = 0.18$ ,  $\gamma_\kappa = -0.93$  and  $\gamma_\rho = 0.77$ .

### III. INVERSION ALGORITHM

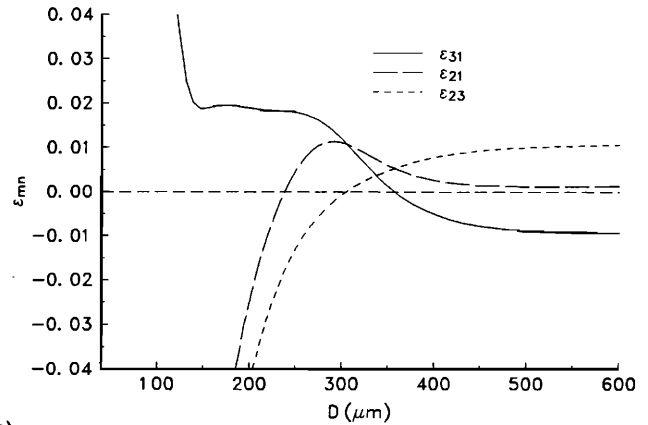
Equation (1) can be rearranged as

$$\frac{\langle v^2 \rangle}{S_M^2 |f_\infty(X)|^2} = \frac{c\tau M_0}{2\rho'_0 a_0}, \quad (8)$$

where  $A, B \sim 0$  for small concentrations of scatterers. Since the concentration and size of particles detected at a particular range should be approximately the same for each channel, then the difference between the left-hand side of



(a)



(b)

FIG. 4.  $\epsilon_{mn}$  versus particle size calculated using 200-set averaged centerline voltages from an experiment using sieved sand with median diameters of (a) 116  $\mu\text{m}$  and (b) 390  $\mu\text{m}$ .

Eq. (8) for different frequency pairs should be small; that is,

$$\frac{\langle v_m^2 \rangle}{(S_M)_m^2 |f_{\infty m}(X_m)|^2} - \frac{\langle v_n^2 \rangle}{(S_M)_n^2 |f_{\infty n}(X_n)|^2} = \epsilon_{mn}, \quad (9)$$

where  $\epsilon_{mn}$  is small, and  $m \neq n$  denote a pair of the three channels. Here,  $m, n = 1, 2$ , and 3 correspond to operating frequencies of 1, 2.25, and 5 MHz, respectively. The left side of Eq. (9) is dependent on particle size and measured quantities, and not concentration explicitly.

The value of  $a$  which minimizes  $|\epsilon_{mn}|$  is an estimate of the mean size in that range bin. In practice, the final size estimate is an average of two zero-crossing locations, so that  $\epsilon_{mn}(a_0) \neq 0$ . Figure 4 shows examples of  $\epsilon_{mn}$  versus diameter from two of the laboratory experiments. Two hundred-set averaged centerline voltages from the three channels using 116- and 390- $\mu\text{m}$ -diam sand [Fig. 4(a) and (b), respectively] were input to Eq. (9) to calculate  $\epsilon_{mn}$  with  $D = 2a$  as an independent variable. An examination of many such plots has shown that a good first estimate of size is given by  $\epsilon_{31} = 0$ . According to whether this estimated diameter is above or below 280  $\mu\text{m}$ , the zero crossing values of  $\epsilon_{23}$  or  $\epsilon_{21}$ , respectively, are used. Figure 4(a) and (b) illustrates these two cases. With increasing size, the zero crossing of  $\epsilon_{21}$  follows the real size of the scatterers to an upper limit of  $D \sim 300 \mu\text{m}$ . Above this size, the

zero crossing of  $\epsilon_{23}$  is a better estimate than  $\epsilon_{21}$ . The multivalued behavior of  $\epsilon_{23}$  for  $D < 280 \mu\text{m}$  leads to ambiguity in the location of the root, as seen in Fig. 4(a). The average of the resulting pair of size estimates is carried forward as the mean size of scatterers in that range bin.

It is assumed here that the size distribution of the particles in suspension has a single dominant size. If the peak in the distribution is ill-defined, or the distribution is bimodal, this inversion technique cannot return meaningful estimates. The naturally occurring distribution at the location of field deployment is unimodal,<sup>11</sup> as is often the case with sandy beach sediments.<sup>23</sup>

Once a mean size has been determined for a particular range bin, concentration is calculated using Eq. (1) for each of the three frequencies. The average of these three estimates is the mean concentration for that bin.

If the final estimate of mean concentration in a particular range bin is above a threshold level (0.1 g/liter, in this case), then the estimated size and concentration are used to calculate the scattering attenuation correction factor, incorporating Eq. (7) in the term  $e^{-A} \sinh B/B$  for each frequency. The reciprocal of this factor is applied as a gain to the square of the voltages in the following bin. Scattering attenuation accumulates with range as regions containing concentrations greater than the threshold are crossed. Concentrations lower than the threshold contribute negligibly.

The approach taken in the ratio algorithm<sup>11</sup> is fundamentally different from the method outlined above. Ratios of measured voltages are matched to lookup tables of theoretical values to extract the size of the scatterers:

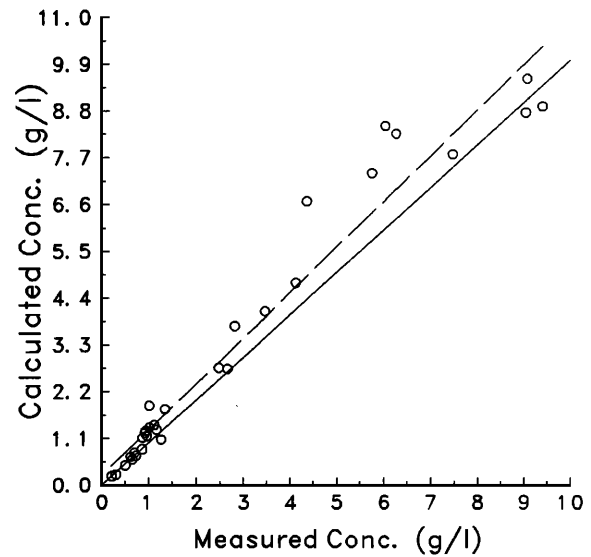
$$\frac{G_i(X, |f_{\infty s}|)}{G_j(X, |f_{\infty s}|)} = \frac{(S_M)_j \langle v_i \rangle}{(S_M)_i \langle v_j \rangle}, \quad (10)$$

where  $i \neq j$  and  $i, j = 1, 2, \text{ or } 3$ , representing the three frequencies. The size-dependent functions  $G_{i,j}$  on the left-hand side are precalculated using the semiempirical form factor  $|f_{\infty s}|$ . This method was found<sup>10,11</sup> to be sensitive to noise, particularly for low signal levels in  $\langle v_j \rangle$ . Also, the inverted sizes obtained from laboratory experiments were found to improve at concentrations above 0.8 g/liter. This is attributed to low signal levels. The difference scheme presented here is not limited in this way.

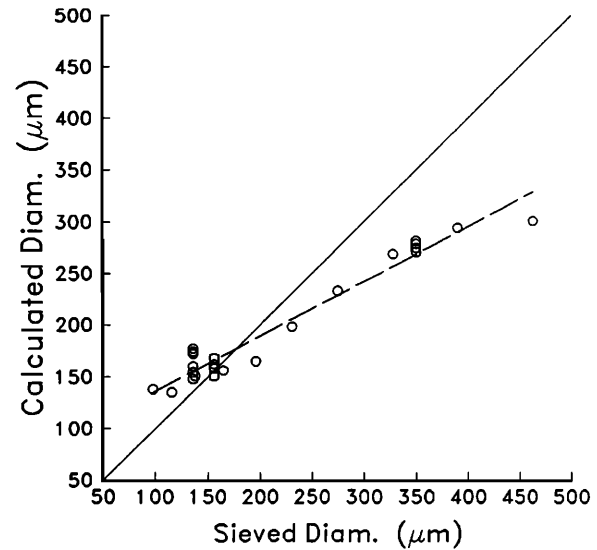
The division of size estimates into two distinct ranges ( $D < 280 \mu\text{m}$  and  $D > 280 \mu\text{m}$ ) is interesting since a similar division is found<sup>10,11</sup> in the ratio inversion scheme, but at  $D = 200 \mu\text{m}$ . This is a consequence of the shape of the form factor. The effect of this on both inversion approaches is that, from three frequencies, only two independent quantities ( $a_0$  and  $M_0$ ) can be determined. A third useful quantity would be  $\sigma_g$ , the standard deviation in the grain size distribution. In this analysis, as in Ref. 10,  $\sigma_g$  has been assumed to be 1.2.

#### IV. LABORATORY RESULTS

The accuracy of the inversion algorithm has been assessed by comparing the calculated sizes and concentrations at the jet centerline to the measured values. Measured and inverted values are plotted against one another in Fig.



(a)



(b)

FIG. 5. Comparison of (a) inverted and measured jet centerline concentration and (b) particle diameter. The solid line is the 1:1 line.

5(a) and (b), with calculated estimates on the vertical axis in both cases. Calculated concentrations are the average of inverted centerline values from 196 jet profiles (a five-set running average has been applied to each 200-set run prior to inversion). Calculated diameters are the average of all nonzero estimates across a 196-set averaged profile, weighted by the number of independent values found at each range bin. Estimates are considered to be independent if they are as far apart in time as the five-set averaging window is wide (that is, 0.75 s or more apart).

Results similar to those presented in Fig. 5 were obtained using the ratio inversion algorithm.<sup>10</sup> The regression statistics for both sets of results are presented in Table III. The two sets of results are similar with both inversion methods tending to slightly overestimate concentration and underestimate the largest sizes. The upper limit of inverted concentrations with the difference algorithm [Fig. 5(a)] is about 10 g/liter. Above this level, the scattering attenuation correction drastically overcorrects the signal levels, as discussed in the Appendix. The ratio algorithm

TABLE III. Regression statistics for comparison of measured and inverted concentration and size using both inversion methods and the semiempirical form factor.

	Concentration		Size	
	Intercept and slope	$R^2$	Intercept and slope	$R^2$
Differences	$0.23 + 1.07x$	0.95	$82.8 + 0.53x$	0.96
Ratio	$-0.04 + 1.10x$	0.97	$43.5 + 0.62x$	0.90

inverts the full range of experimental concentrations (up to 23 g/liter). In the case of the very largest sand sizes, some of the underestimation may be real, due to settling of the largest particles in the jet recirculation system. Sizes estimated by the difference algorithm have a tendency to increase with concentration [seen in the series of size estimates for sand with diameters 139, 157, and 390  $\mu\text{m}$ , Fig. 5(b)]. The opposite tendency is shown by the ratio algorithm. The regression statistics quoted for the ratio algorithm results include all laboratory experiments: If only those runs with concentration over 0.8 g/liter are included,  $R^2=0.98$  for concentration estimates and 0.94 for size estimates.

Comparison between inverted results using the two approximations to the backscattering form factor has been made using a calculation neglecting the scattering attenuation correction. The effect of attenuation, increasing with scatterer concentration, is clearly evident in Fig. 6(a). Concentrations obtained using  $|f_{\infty r}|$  are larger than those values estimated using the semiempirical form factor. The regression fit to the estimated sizes using  $|f_{\infty r}|$  has slope closer to the 1:1 line.

### A. Averaging

Averaging is necessary to remove purely statistical variations due to the random relative motion of the scatterers. However, by correlating signal levels at two streamwise-separated points, it has been shown<sup>13</sup> that large fluctuations in the backscattered intensity from the jet represent real structure in the concentration field. Similar fluctuations are seen in field data,<sup>15</sup> where these can contribute significantly to sediment flux.

One would like to know how much averaging is required to provide stable concentration estimates, but still resolve the fluctuations of interest. This question is addressed here by examining the variability in the inversion estimates from laboratory runs using sieved sand. The size fractions are narrow, so one would expect the real (non-statistical) variability to be due mainly to concentration fluctuations.

Figure 7 shows standard deviation as a function of the square root of the number of sets in the preprocessing averaging window at a range of 53.0 cm (two range bins toward the transducers from the jet center) for three different experimental runs, without the scattering attenuation correction. For these runs, at 53.0 cm, the diameter estimation was robust. (In the case where signal levels are low enough that inversion is not attempted, zero diameter

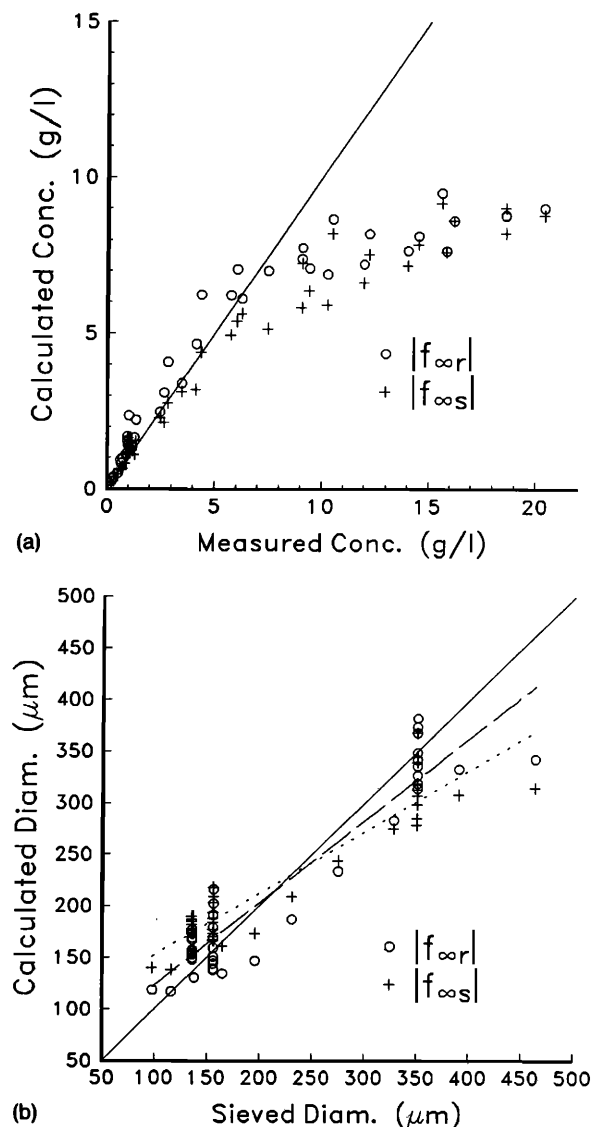


FIG. 6. Comparison of (a) inverted and measured jet centerline concentration and (b) particle diameter using  $|f_{\infty r}|$ , and neglecting the scattering attenuation correction. In both parts of the figure, O denotes values calculated using  $|f_{\infty r}|$  (with dashed line linear regression fit) and + denotes values calculated using  $|f_{\infty s}|$  (dotted line linear regression).

values are returned by the algorithm. Null entries are not included in the averaged size profiles, whereas null concentrations are meaningful, so the number of independent diameter estimates is potentially lower than the number of independent concentration estimates, but not at this range in the runs used here.) Runs 011, 014, and 017 used sand with  $d_{50}=165, 196,$  and  $231 \mu\text{m}$ , respectively, and centerline concentrations of about 1 g/liter.

With the scaling used in Fig. 7, one would expect a linear decrease ( $1/\sqrt{n}$ ) in standard deviation as the number of sets averaged increases. The data in the figure are roughly consistent with this behavior, particularly for  $n > 4$ , and arguably moreso for size than for concentration. The variability in the size estimates does fall off more rapidly than that for concentration. The standard deviation in particle diameter has been reduced to approximately 10% of the mean after preaveraging the voltage data over as few

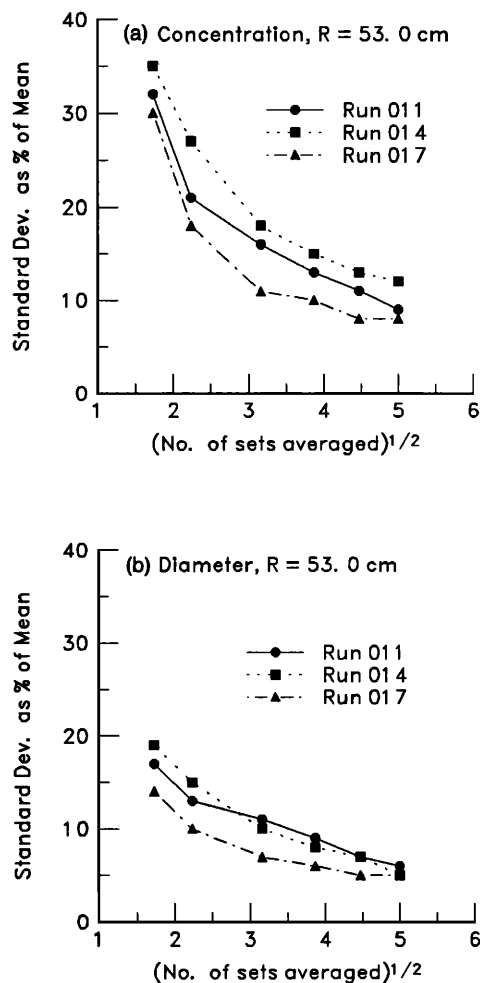


FIG. 7. Standard deviation as a function of preaveraging window size. (a) Concentration and (b) diameter statistics are plotted as a percentage of the mean value in each case.

as ten sets. The standard deviation in concentration is less than 20% of the mean with this amount of preaveraging. As mentioned earlier, the concentration field in the jet contains large real turbulent fluctuations, whereas the widths of the sieved sand size distributions are narrow. Larger variability in the concentration estimates is therefore to be expected.

The size and concentration estimates presented earlier were computed from voltage data to which a five-set running average was applied. Figure 7 shows the standard deviation in this case to be typically about 15% in diameter, and 25% in concentration.

## V. FIELD RESULTS

Comparison of inverted field data will be made with results obtained using the ratio algorithm and with OBS data, and using both approximations to the backscatter form factor.

### A. Comparison of inverted concentrations with OBS measurements

Voltage data from the field experiments were averaged over a 1.1-s (seven-set) interval to reduce fluctuations in

TABLE IV. Distances for RASTRAN-OBS133 concentration comparisons:  $h_{\text{OBS}}$  is distance from OBS133 to bottom and  $r_{\text{OBS}}$  is taken from the 5 MHz (reference) unit to the center of the range bin compared with OBS133 data.

Run	$h_{\text{OBS}}$ (cm)	$r_{\text{OBS}}$ (cm)
300.030	5.0	87.8
301.015	4.8	87.8
308.046,.047	9.5	87.6

the backscatter signal due to relative motion of the scatterers, and to lessen the effects of the horizontal separation of the transducers. Entire runs and segments of runs representing varying levels of suspension activity were averaged and compared with OBS measured concentrations averaged over the same time intervals. The ranges ( $r_{\text{OBS}}$ ) at which to compare the inverted results with the OBS133 data, as determined in Ref. 10, are listed in Table IV. Changes in distance to bottom ( $h_{\text{OBS}}$ ) are due mainly to the migration of bedforms.<sup>24</sup> Small changes in  $r_{\text{OBS}}$  are due to changes in the local sound speed (mainly temperature dependent) which alter the spatial placement of the time-gated range bins. OBS134 and OBS135 were located 5 and 10 cm above OBS133. The range to OBS135 fell between range bins so RASTRAN concentration values reported are the average of the values in the flanking bins. For purposes of comparison with earlier results obtained with the ratio algorithm,<sup>10</sup> inverted values were computed using the semiempirical form factor. Results computed with the rational fraction fit are discussed later.

The RASTRAN/OBS comparisons of run-averaged concentrations are shown in Fig. 8, for the same runs as in Ref. 10. For the bottom OBS, there is a slight overestimation of concentration [Fig. 8(a)]. Note that the laboratory data [Fig. 5(a)] show a similar effect. The scatter in the results increases with height above bottom, with low and intermediate energy runs plotting below the 1:1 line, and high energy runs above. Similar variations with height were noted in the ratio results,<sup>10</sup> and were attributed to the effects of fine particles in suspension, to which the OBS is very sensitive. Overall, these results represent improved agreement between the RASTRAN and OBS estimates of concentration, compared to those obtained using the ratio algorithm,<sup>10</sup> especially at the higher levels.

### B. Averaged size and concentration profiles

Profiles of mean concentration and size are shown in Fig. 9 for both approximations to the form factor. Also shown are the mean size and concentration profiles obtained with the ratio algorithm and the semiempirical form factor. Each profile represents the average of runs 299.025–.028, during intermediate energy wave conditions (Table II). The profiles are not considered accurate below 5-cm height due to variable bottom echo contamination of the backscatter signal among the sounders (ripple bedforms approximately 2 to 3 cm in height and with wavelengths between 5 and 15 cm were present at the RASTRAN site

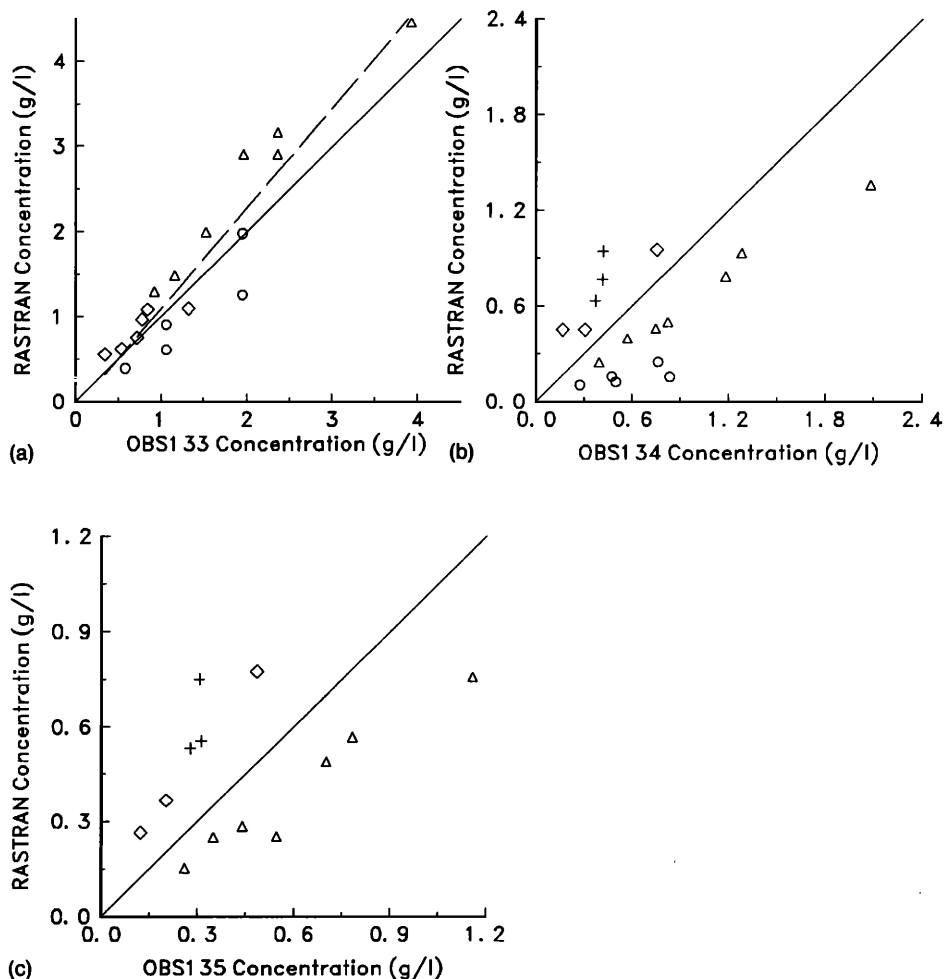


FIG. 8. Comparison between inverted and OBS measured concentrations at three levels above bottom. For part (a), distance from bottom to OBS133 is listed in Table IV. (b) OBS134 and (c) OBS135 are 5 and 10 cm above OBS133, respectively.  $\circ$  and  $\Delta$  are from low and intermediate energy runs and  $+$  and  $\diamond$  are from high energy runs. The dashed line in (a) is the linear regression fit to all points in that graph.

during the field deployment<sup>24</sup>) and the inevitable presence of some suspended material near the bottom in the background profiles.

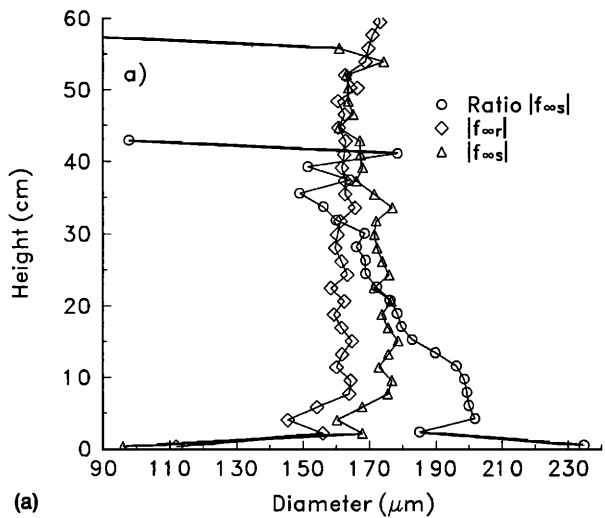
The concentration profiles are shown in Fig. 9, using both linear and log-log scaling. The error bars represent  $\pm 1$  standard error based on the variance of the estimates for the four runs. In all cases these error bars are  $< 5\%$ – $10\%$  of the mean, indicating little variance in the mean profile between runs. In the region above 35-cm height, the effect of subtraction of a background level in the difference algorithm is evident in reduced concentrations compared to the ratio results. Below 35 cm height, concentrations estimated by the difference algorithm are larger than those from the ratio algorithm, by as much as a factor of 2. These higher concentrations are the reason for the improved agreement with the OBS data (Fig. 8, compared to Ref. 10). Note that the concentration estimates are sensitive to the choice of form factor, evident from the difference algorithm results for the rational fraction and semiempirical fits, even though these fits differ by only 0(10%) in this  $ka$  range: 0.3 to 2 for the bottom sediment size of  $170 \mu\text{m}$  (see the discussion of size estimates below, and Fig. 3).

The log-log plot [Fig. 9(b)] indicates that in the bot-

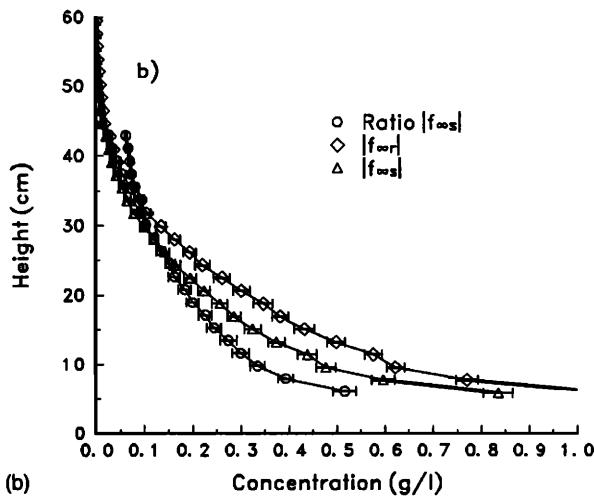
tom 15–20 cm of the profile, concentration decays with height following a power law. The wave boundary layer thickness<sup>25</sup> is approximately 10–20 cm, and a power law dependence of concentration on height in this layer is predicted by some sediment transport models.<sup>25,26</sup> The two inversion algorithms produce quite different behavior at heights above bottom greater than 20 cm. (The difference algorithm results decay more rapidly.) This is partly a background subtraction effect, and partly due to the problems with the ratio algorithm at low concentrations.

The size profiles are shown in Fig. 10. At 10-cm height, the mean diameter is about  $165 \mu\text{m}$  for the rational fraction form factor, and  $175 \mu\text{m}$  for the semiempirical form factor. These sizes agree well with the  $170\text{-}\mu\text{m}$  median size of the sand sample taken from the bed at the deployment site. The  $10\text{-}\mu\text{m}$  difference in the estimates using the two different form factors is consistent with the laboratory findings for estimation of sizes near  $170 \mu\text{m}$  [Fig. 6(b)]. This size also happens to fall in the region where size estimation is best [Fig. 5(b)] so no correction has been made to the calculated values.

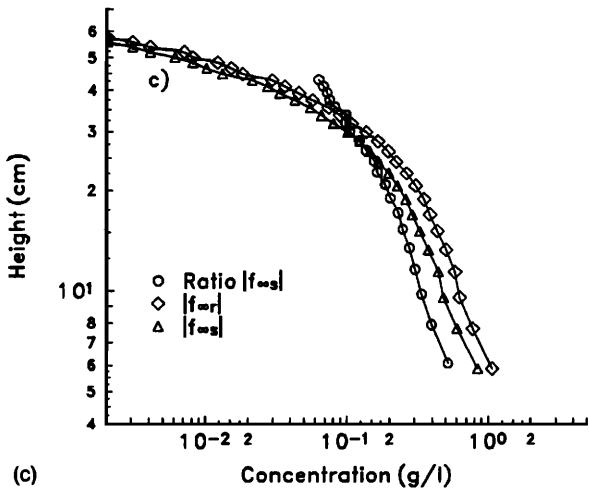
The ratio estimate of diameter at 10-cm height is  $200 \mu\text{m}$ . This value is 20% higher than the bottom sediment



(a)



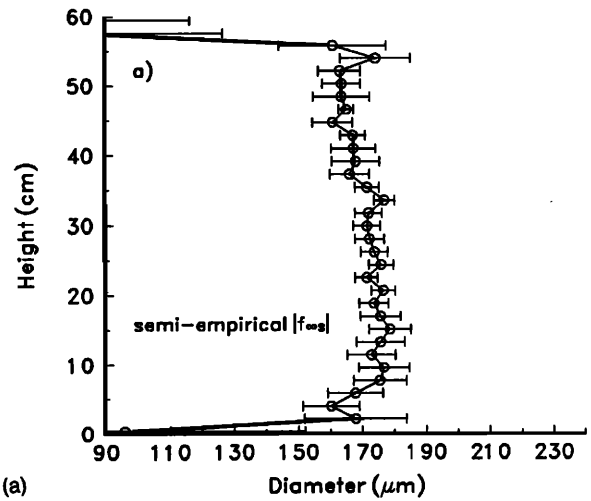
(b)



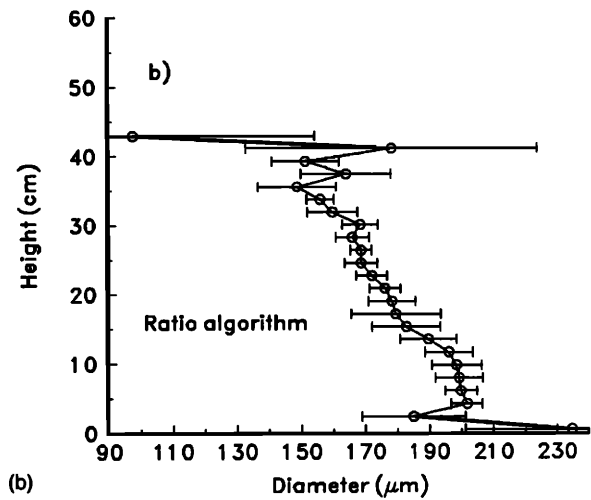
(c)

FIG. 9. Four-run averaged profiles of (a) size, and (b) and (c) concentration for runs 299.025-.028 using both form factors and the ratio algorithm.

size, which is acceptable but less accurate in this sense than the difference result. The two algorithms indicate different functional dependence of mean size on height, however. This is demonstrated by Fig. 10(b) and (c), which shows the profiles of size from the ratio and difference algorithms



(a)



(b)

FIG. 10. Four-run averaged profiles of size with error bars denoting plus or minus one standard error for runs 299.025-.028 using the difference algorithm with the (a) semiempirical form factor and using (b) the ratio algorithm.

with the semiempirical fit for the form factor in both cases. The error bars represent the standard error of the estimate, as in Fig. 9(a). The error bars are somewhat smaller for the difference results, and are less than 7% between 5 and 50 cm in height. Above 5-cm height, the difference estimates exhibit nearly uniform size, with only a very slight linear decay, about 8% over 50 cm. The linear decay in the ratio estimates is greater, representing a 25%–30% change over 50 cm. As noted previously,<sup>10</sup> measurements of suspended sand size made by direct sampling<sup>9</sup> in the near-shore zone indicate a 15%–25% decrease over 50 cm. One conclusion is that the multifrequency results from both inversion methods are equally consistent with the available direct sampling measurements.

Figure 11 shows the percentage difference as a function of height between the averaged profiles obtained from the difference algorithm, using the two fits to the form factor data. Up to a height of about 30 cm, the difference in size is approximately constant, and small: about -8%. The concentration differences are also approximately constant, but much larger: about 25% over the same height

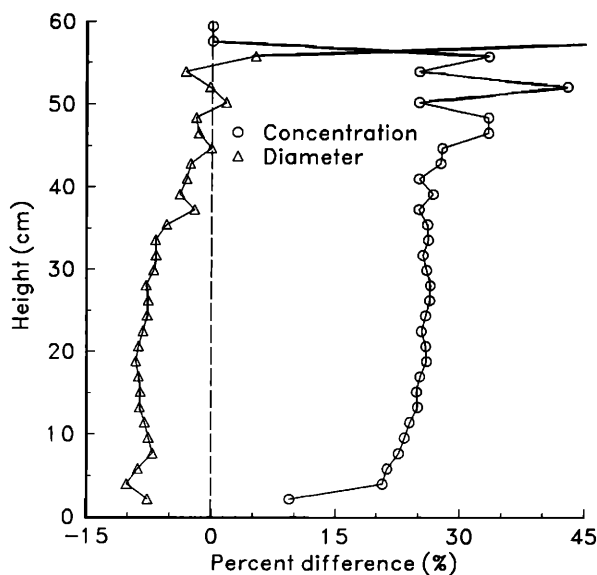


FIG. 11. Percent difference between size and concentration estimates using the two different form factors.

range. This sensitivity of the concentration estimate to small changes in the form factor can be qualitatively understood by examining Eq. (8). The concentration  $M$  at a given frequency depends on the ratio  $a_0/|f_\infty|^2$ . Since  $|f_\infty|$  decreases as  $a_0$  decreases over the  $X$  range of interest (Fig. 2), larger concentrations are expected for smaller size estimates, as shown in Fig. 11. The fact that the percentage change in concentration is roughly three times that in size is due to the nonlinear dependence of  $|f_\infty|$  on size. This dependence will be different at each frequency. In the Rayleigh region (i.e., at 1 MHz), for example, the above ratio would go as  $a_0^{-3}$ , which would translate into a three-fold amplification of the size difference.

### C. Factors affecting $|f_\infty|$

The results of the previous section demonstrate that the concentration estimates are sensitive to small differences in the backscatter cross section. It is therefore relevant to consider factors which might lead to natural variations in  $f_\infty$  for sand. One such factor is sand grain mineralogy. This is illustrated in Fig. 12(a). Shown is the backscattering form factor as a function of  $X$  for garnet and quartz spheres. Quartz is perhaps the most common mineral on sand beaches. Garnet is an example of a typical heavy mineral. The physical properties for these materials, taken from Ref. 27, are listed in Table V. Note that the sound speeds listed are averages of measurements along the different axes of single crystals, appropriately weighted to represent the speeds in the polycrystalline form of the pure mineral. Other estimates which might be used are those based on measurements of the elastic constants for quartz-bearing rocks at atmospheric pressure.<sup>28</sup> Included in Table V is one such entry, for granite. These speeds are lower than for pure quartz and garnet mainly because of defects in the rock. Another possible set of values is that for fused quartz,<sup>29</sup> although the density of this material is lower than

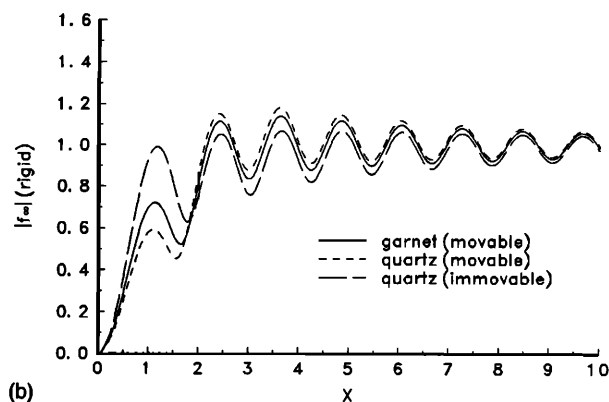
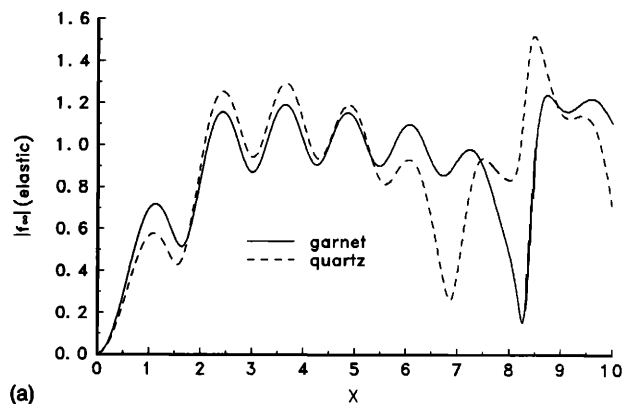


FIG. 12. Backscattering form factor for garnet and quartz (physical parameters are listed in the text): (a) the elastic scatterer case and (b) the rigid, movable case.

is typical of beach sand. The point is that precise values for the elastic constants (i.e., sound speeds) for sand grains are not well known.

The elastic sphere calculations show a large shift in the position of the first resonance, the oblate-prolate mode, from below  $X=7$  for quartz to above  $X=8$  for garnet. This shift is sensitive mainly to the shear velocity of the material.<sup>30</sup> The measurements for sand lie well below the resonance, for both materials (Fig. 2). The measurements do not exhibit the oscillations predicted by spherical scatterer theory in the region below the first resonance, except in the vicinity of  $X=1$ . The amplitude of the  $X=1$  peak is due in part to the motion of the scatterer about its center of mass,<sup>17,18</sup> and therefore depends on the bulk density of the scatterer relative to the medium. This is illustrated in Fig. 12(b), which shows the form factor computed for rigid spheres with infinite density (the immovable case), and with the densities of quartz and garnet. In the region  $X \sim 1$ , there is a difference of up to 25% between the quartz and garnet curves. According to the results of the previous section, this difference is enough to significantly affect the concentration estimates. This suggests that variations in grain density may need to be taken into account in some

TABLE V. Bulk densities, compression ( $c_p$ ) and shear ( $c_s$ ) wave velocities for different minerals.

Material	$\rho_0$ ( $\text{kg/m}^3$ )	$c_p$ ( $\text{m/s}$ )	$c_s$ ( $\text{m/s}$ )
Garnet	4249	8480	4760
Quartz	2649	6050	4090
Granite	2670	4800	3200
Fused quartz	2200	5900	3750

cases, and that the sand grain bulk density should be routinely measured in the field.

The absence of diffraction oscillations above  $X=1$  in the measurements (compare Figs. 2 and 12) is likely due to the irregular shapes of natural sand grains<sup>13</sup> as the measurements were obtained from experiments using sieved sands with narrow size distributions. Measurements for nearly spherical glass beads sieved into the same size fractions with the same set of sieves do exhibit these oscillations clearly.<sup>13</sup> Irregularities in grain shape would also detune the resonances. Figure 13 shows the rigid movable and elastic quartz sphere cases, smoothed with a log-normal size distribution with width  $\sigma_g=1.2$  [Eqs. (4) and (5)], as well as the rational fraction fit to the experimental data. It is interesting that including elasticity leads to improved agreement with the measurements for  $1.5 < X < 4.5$ .

#### D. Other sources of error

Contamination of the backscatter signal by biological or other nonsedimentary scatterers is a potential source of error in acoustic measurements of suspended sediment. In the surf zone, bubbles represent the most serious problem of this type. The particular runs analyzed here were selected in part for lack of obvious bubble contamination, which in our experience is indicated by a persistent increase in the background signal level, and increasing signal levels with increasing distance from the bed. The good agreement obtained between RASTRAN and OBS estimates of concentration also indicates that bubble contamination was not a serious problem for the runs presented here, in light of the very different relative sensitivities of these devices to bubbles and sand. Signal contamination by bubbles nevertheless remains an outstanding problem in the application of acoustic techniques for suspended sediment measurements in the surf zone.

The difference algorithm, as implemented here, does not take into account the particle size distribution. The estimates of mean size are weighted by the product of the backscatter cross section and the size spectral density, and will therefore differ from the true mean. We have assumed that this difference is not large, provided the sand size distribution is well behaved, i.e., not bimodal, and not too broad. The consistency of the size estimates with the bottom sediment median size supports this assumption. The assumption of a single dominant size was also necessary for practical reasons. Computation time is already long (the current version of the algorithm takes 1 h on a workstation to process a 2600-set run), and would be significantly in-

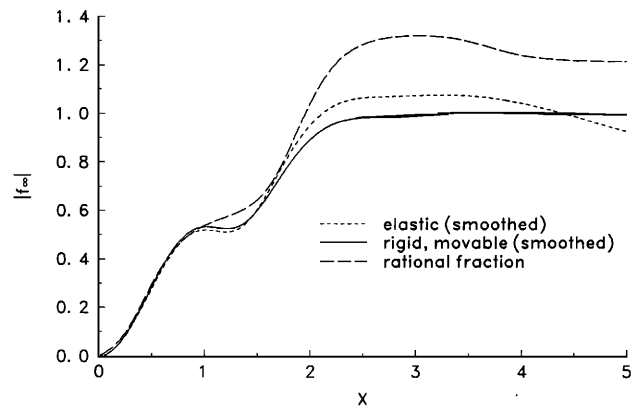


FIG. 13. Smoothed form factors for garnet and quartz, with the rational fraction fit to the measured data.

creased if several size fractions were included. This is a limitation of the present approach. Information on the size distribution, particularly on its variations with height above bottom, would clearly be useful in sediment transport applications. This study suggests that more than three frequencies would be beneficial for this purpose, but that more efficient difference-minimization techniques would need to be implemented.

#### VI. CONCLUSIONS

Comparison of inverted and measured laboratory data shows that the inversion algorithm is reasonably accurate over the range of particle sizes used in the experiments (98- to 463- $\mu\text{m}$  diameter) at concentrations up to 10 g/liter. A significant result arising from the examination of the laboratory data is the identification of a large overcorrection by the scattering attenuation term at high concentrations, although this does not impair the usefulness of the algorithm with the field data. Future implementation of another frequency less sensitive to scattering attenuation, i.e., below 5 MHz, would be advantageous.

A goal of this work has been to develop an alternate method of inverting backscatter data which is less sensitive to low signal levels than the ratio technique. The half-hour-averaged profiles shown in Fig. 9 demonstrate that this has been accomplished. The inverted vertical profiles from the field data extend farther from the bottom into regions of lower concentration. As well, the standard error in size is less than 7% through most of this range. In general, this error is less than for similar profiles from the ratio algorithm, and the region of lower standard error extends over a larger vertical range.

The differences in the inverted results using two fits to the backscattering form factor data show that estimates of size and concentration can be sensitive to small differences in this parameter. For the particular case discussed, with sand of diameter 170  $\mu\text{m}$ , an approximately 10% difference between the two form factors (at 2.25 and 5 MHz) results in an 8% difference in the estimated size, and a 25% difference in the estimated concentration.

## ACKNOWLEDGMENTS

This work was conducted as part of a Master's degree in the Physics Department at Memorial University of Newfoundland.<sup>31</sup> The authors thank Dr. Jinyu Sheng for helpful discussions of his work, and Dr. John Lewis, Memorial University, who suggested the rational fraction fit. One of us (AMC) was supported by a graduate fellowship from Memorial University of Newfoundland. The work was funded by the Operating and Strategic Grants programs of the Natural Sciences and Engineering Research Council of Canada.

## APPENDIX: EXAMINATION OF SCATTERING ATTENUATION

The attenuation correction factor has been tested by comparison with laboratory measurements of attenuation. A small hydrophone was placed opposite the 2.25-MHz unit at range  $r_H$ , as described in Ref. 13. The ratio of the voltage output,  $v_H$ , from the hydrophone with the pump system off and on represents the one-way attenuation due to particles across the full width of the jet:

$$\frac{A}{2} = \ln \left( \frac{v_H(M_c=0)}{v_H(M_c)} \right), \quad (\text{A1})$$

where  $M_c$  is the measured centerline concentration. These values represent half the accumulated attenuation [Eqs. (7) and (2)] at a range bin corresponding to approximately  $r_H$ . For each of two sand sizes, 360  $\mu\text{m}$  (QLB) and 139  $\mu\text{m}$  (BWB), measured and calculated  $A/2$  are plotted, with regression fits (Fig. A1), as a function of measured centerline concentration. The calculated values are approximately twice as large as the measured values. This discrepancy leads to failure of the difference algorithm when the concentration is larger than 10 g/liter over several range bins.

When high concentration levels are encountered, overcorrection for scattering attenuation occurs—in cases of high mean concentration, the effect accumulates across the

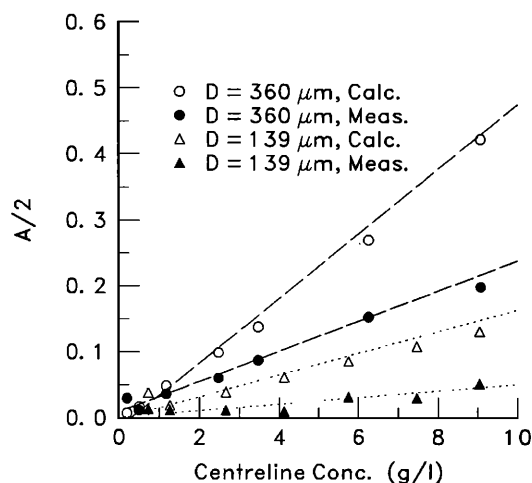


FIG. A1. Measured and calculated scattering attenuation, accumulated across the full width of the jet. Measured values are shown by filled symbols, and calculated values by open symbols.

jet until failure occurs when corrected signal levels blow up exponentially, particularly in the 5-MHz channel. Similar overcorrection of the squared mean backscatter intensity from sand in suspension has been noted at MHz frequencies.<sup>12,32</sup> The problem appears to be a result of the way that the scattering attenuation correction is applied, rather than with the high-pass model for  $\alpha_s$ , since total scattering cross sections for natural sand grains computed from the measured attenuation in the jet agree well with this model.<sup>12</sup> Thorne *et al.*<sup>7</sup> have used the same high-pass model for  $\alpha_s$ , obtaining good results for particle diameters of 210, 125, and 55  $\mu\text{m}$  at 3 MHz, though the concentrations used were low: between 0.01 and 1 g/liter—for which scattering attenuation effects remained small. As pointed out by Thorne *et al.*,<sup>32</sup> similar overcorrection problems found in downward-looking radar backscatter estimates of rainfall rate have been dealt with by normalizing to the surface echo.<sup>33</sup> The surface reflection coefficient is assumed to remain constant. Whether or not this assumption would be valid during active sediment suspension events in the nearshore zone is unclear. Regardless, this approach was not feasible here, since the bottom echo saturated the receiver.

Having discussed this shortcoming of the algorithm at length, it should be pointed out that the inverted results for the jet experiments with centerline concentrations less than 10 g/liter are quite good [Fig. 5(a) and (b)]. Mean concentration levels in the field data rarely exceed 10 g/liter, except very near the bottom, and this type of failure was not encountered in the field data inversions.

<sup>1</sup>R. A. Young, J. T. Merrill, T. L. Clarke, and J. R. Proni, "Acoustic Profiling of Suspended Sediments in the Marine Bottom Boundary Layer," *Geophys. Res. Lett.* **9**, 175–178 (1982).

<sup>2</sup>J. F. Lynch, "Theoretical Analysis of ABSS data for HEBBLE," *Mar. Geol.* **66**, 277–289 (1985).

<sup>3</sup>D. M. Hanes, C. E. Vincent, D. A. Huntley, and T. L. Clarke, "Acoustic Measurements of Suspended Sand Concentration in the C<sup>2</sup>S<sup>2</sup> Experiment at Stanhope Lane, Prince Edward Island," *Mar. Geol.* **81**, 185–196 (1988).

<sup>4</sup>C. Libicki, and K. W. Bedford, "The Interpretation and Evaluation of a 3-MHz Acoustic Backscatter Device for Measuring Benthic Boundary Layer Sediment Dynamics," *J. Acoust. Soc. Am.* **85**, 1501–1511 (1989).

<sup>5</sup>J. F. Lynch, T. F. Gross, B. H. Brumley, and R. A. Filyo, "Sediment Concentration Profiling in HEBBLE using a 1-MHz Acoustic Backscatter System," *Mar. Geol.* **99**, 361–385 (1991).

<sup>6</sup>C. E. Vincent, D. M. Hanes, and A. J. Bowen, "Acoustic Measurements of Suspended Sand on the Shoreface and the Control of Concentration by Bed Roughness," *Mar. Geol.* **96**, 1–18 (1991).

<sup>7</sup>P. D. Thorne, C. E. Vincent, P. J. Hardcastle, S. Rehman, and N. Pearson, "Measuring Suspended Sediment Concentrations Using Acoustic Backscatter Devices," *Mar. Geol.* **98**, 7–16 (1991).

<sup>8</sup>J. F. Lynch and Y. C. Agrawal, "A Model-Dependent Method for Inverting Vertical Profiles of Scattering to Obtain Particle Size Spectra in Boundary Layers," *Mar. Geol.* **99**, 387–401 (1991).

<sup>9</sup>P. Nielsen, M. O. Green, and F. C. Coffey, "Suspended Sediment under Waves," *Tech. Rep. 82/6*, 157 pp., Coastal Stud. Unit, Univ. of Sydney, Sydney, Australia (1982).

<sup>10</sup>A. E. Hay, and J. Sheng, "Vertical Profiles of Suspended Sand Concentration and Size From Multifrequency Acoustic Backscatter," *J. Geophys. Res.* **97**(C10), 15,661–15,677 (1992).

<sup>11</sup>J. Sheng, "Remote Determination of Suspended Sediment Size and Concentration by Multi-frequency Acoustic Backscatter," Ph.D. thesis, Dept. of Physics, Memorial University of Nfld. (1991).

<sup>12</sup>A. E. Hay, L. Huang, E. B. Colbourne, J. Sheng, and A. J. Bowen, "A

- High Speed Multi-Channel Data Acquisition System for Remote Acoustic Sediment Transport Studies," in *Oceans '88 Proceedings* (IEEE, Baltimore, 1988), Vol. 2, pp. 413-418.
- <sup>13</sup> A. E. Hay, "Sound Scattering from a Particle-Laden, Turbulent Jet," *J. Acoust. Soc. Am.* **90**, 2055-74 (1991).
- <sup>14</sup> R. E. Carver (Ed.), *Procedures in Sedimentary Petrology* (Wiley, New York, 1971) 653 pp.
- <sup>15</sup> A. E. Hay and A. J. Bowen, "On the Coherence Scales of Wave-Induced Suspended Sand Concentration Fluctuations," *J. Geophys. Res.* (to be published).
- <sup>16</sup> D. G. Hazen, D. A. Huntley, and A. J. Bowen, "UDATS: A System for Monitoring Nearshore Processes," *Proc. Oceans '87*, 993-997 (1987).
- <sup>17</sup> A. E. Hay and A. S. Schaafsma, "Resonance Scattering in Suspensions," *J. Acoust. Soc. Am.* **85**, 1124-1138 (1989).
- <sup>18</sup> A. E. Hay and D. G. Mercer, "On the Theory of Sound Scattering and Viscous Absorption in Aqueous Suspensions at Medium and Short Wavelengths," *J. Acoust. Soc. Am.* **78**, 1761-1771 (1985).
- <sup>19</sup> Cheng He and A. E. Hay, "Broadband Measurements of the Acoustic Backscatter Cross Section of Sand Particles in Suspension," *J. Acoust. Soc. Am.* **94**, 2247-2254 (1993).
- <sup>20</sup> R. W. Hornbeck, *Numerical Methods* (Prentice-Hall, Englewood Cliffs, NJ, 1975), p. 128.
- <sup>21</sup> J. Sheng and A. E. Hay, "An Examination of the Spherical Scatterer Approximation in Aqueous Suspensions of Sand," *J. Acoust. Soc. Am.* **83**, 598-610 (1988).
- <sup>22</sup> R. K. Johnson, "Sound Scattering from a Fluid Sphere Revisited," *J. Acoust. Soc. Am.* **61**, 375-377 (1977).
- <sup>23</sup> P. D. Komar, *Beach Processes and Sedimentation* (Prentice-Hall, Englewood Cliffs, NJ, 1976).
- <sup>24</sup> A. E. Hay and A. J. Bowen, "Spatially Correlated Depth Changes in the Nearshore Zone during Autumn Storms," *J. Geophys. Res.* **98**(C7), 12387-12404 (1993).
- <sup>25</sup> S. M. Glenn and W. D. Grant, "A Suspended Sediment Stratification Correction for Combined Wave and Current Flows," *J. Geophys. Res.* **92**, 8244-8264 (1987).
- <sup>26</sup> C. E. Vincent and M. O. Green, "Field Measurements of the Suspended Sand Concentration Profiles and Fluxes and of the Resuspension Coefficient  $\gamma_0$  over a Rippled Bed," *J. Geophys. Res.* **95**(C7), 11591-11601 (1990).
- <sup>27</sup> R. S. Carmichael (Ed.), *Practical Handbook of Physical Properties of Rocks and Minerals* (CRC, Boca Raton, FL, 1989).
- <sup>28</sup> S. P. Clarke, "Handbook of Physical Constants," *Geol. Soc. Am. Mem.* **97**, revised edition, 197-201 (1966).
- <sup>29</sup> R. C. Weast (Ed.), *CRC Handbook of Chemistry and Physics* (CRC, Boca Raton, FL, 1984), 65th ed.
- <sup>30</sup> L. Flax, G. C. Gaunard, and H. Überall, "Theory of Resonance Scattering," in *Physical Acoustics*, edited by W. P. Mason and R. N. Thurston (Academic, New York), Vol. XV, pp. 191-294.
- <sup>31</sup> A. M. Crawford, "A Comparison of Two Inversion Methods for Determination of Sand Concentration and Size from Multifrequency Acoustic Backscatter," M.Sc. thesis, Dept. of Physics, Memorial University of Nfld. (1992).
- <sup>32</sup> P. D. Thorne, P. J. Hardcastle, and R. L. Soulsby, "Analysis of Acoustic Measurements of Suspended Sediments," *J. Geophys. Res.* **98**(C1), 899-910 (1993).
- <sup>33</sup> M. Marzoug and P. Amayenc, "Improved Range-Profiling Algorithm of Rainfall Rate from a Spaceborne Radar with Path-Integrated Attenuation Constraint," *IEEE Trans. Geosci. Remote Sensing* **29**(4), 584-592 (1991).